

Cite this: *J. Mater. Chem. A*, 2017, 5, 21570

# Plasmonic enhanced photoelectrochemical and photocatalytic performances of 1D coaxial Ag@Ag<sub>2</sub>S hybrids†

Nan Zhang,<sup>a</sup> Mingjie Li,<sup>d</sup> Chuan Fu Tan,<sup>a</sup> Connor Kang Nuo Peh,<sup>a</sup>  
Tze Chien Sum<sup>d</sup> and Ghim Wei Ho<sup>\*,abc</sup>

Silver (Ag) as one of the most important plasmonic metals has attracted enormous attention due to its distinct surface plasmon resonance (SPR) absorption and high electrical conductivity. Here, we use Ag nanowires (NWs) as the starting material to prepare a series of core-shell structured Ag@Ag<sub>2</sub>S composites through an *in situ* controllable and spontaneous sulfidation process at room temperature. It has been found that the obtained coaxial Ag@Ag<sub>2</sub>S hybrid with an optimized ratio of Ag NWs exhibits enhanced photoelectrochemical and photocatalytic performances under visible light irradiation. The underlying contribution of Ag SPR to the enhancement of photoelectrochemical and photocatalytic activities of the Ag@Ag<sub>2</sub>S hybrids has been elucidated through wavelength-dependent experiments and transient absorption spectroscopy. The results indicate that the SPR phenomenon of Ag NWs has an influential effect on the photoelectrochemical and photocatalytic activities enhancement of Ag@Ag<sub>2</sub>S hybrids, which is often overlooked in the previous reports. An ultrafast electron transfer process (~350 fs) from the Ag core to the Ag<sub>2</sub>S shell has been measured. This work provides a valuable insight into the role of the Ag component in improving the photoelectrochemical and photocatalytic performances of Ag–Ag<sub>2</sub>S hybrid nanosystems, which is expected to promote comprehensive understanding and better exploitation of plasmonic Ag in universal photophysical and photochemical systems.

Received 24th July 2017  
Accepted 14th September 2017

DOI: 10.1039/c7ta06473j

rsc.li/materials-a

## Introduction

Metal–semiconductor hybrid nanostructures have attracted extensive attention due to their synergistic properties and performances that essentially result from interactions between the disparate metal and semiconductor components.<sup>1–5</sup> Among numerous metal–semiconductor heterostructured nanosystems, those comprising plasmonic metals and semiconductors combined within specific nanoarchitectures represent a class of promising paradigms, which have found various applications in the fields of electronics,<sup>6</sup> optics,<sup>7</sup> biotechnology,<sup>8</sup> solar cells,<sup>9</sup> and photocatalysis.<sup>10</sup>

Silver (Ag) as one of the most studied plasmonic metals, not only exhibits distinct and tunable surface plasmon resonance (SPR) absorption, but also has the highest electrical

conductivity ( $6.3 \times 10^7 \text{ S m}^{-1}$ ) among all metals.<sup>11,12</sup> Owing to these intriguing optical and electrical properties, Ag has been considered as a promising candidate for constructing high-performance composite photocatalysts. Thus far, there have been various Ag-based nanostructured photocatalysts, such as Ag nanocube/N-doped TiO<sub>2</sub> composites,<sup>13</sup> Ag–ZnO heterostructured nanofibers,<sup>14</sup> Ag nanowire/Ag<sub>3</sub>PO<sub>4</sub> cube necklace-like heterostructures,<sup>15</sup> Ag@Cu<sub>2</sub>O core-shell nanoparticles,<sup>16</sup> Ag@AgCl cubic cages,<sup>17</sup> Ag–Sb<sub>2</sub>S<sub>3</sub> hollow microspheres,<sup>18</sup> Ag/Ag<sub>2</sub>S heterodimers,<sup>19</sup> *etc.*<sup>20–24</sup>

Of the known Ag–semiconductor hybrid nanostructured photocatalysts, Ag–Ag<sub>2</sub>S is of particular interest<sup>25,26</sup> because Ag<sub>2</sub>S is a direct semiconductor with a narrow band gap (*ca.* 1.0 eV), a high optical absorption coefficient, chemical stability and nontoxicity.<sup>27–31</sup> Diverse Ag–Ag<sub>2</sub>S hybrids with different nanostructures have been synthesized and applied for photo-redox processes, including antibacterial, degradation of organic dyes, and reduction of heavy ions.<sup>19,20,25,31–34</sup> For example, Zeng *et al.*<sup>19</sup> have developed an ion exchange and photo-assisted reduction method to prepare Ag–Ag<sub>2</sub>S heterodimers at room temperature. The highly asymmetric Ag<sub>2</sub>S/Ag heterodimers exhibited strong bactericidal effects on *E. coli* K-12 under UV irradiation, which was attributed to the synergetic effects of both Ag<sub>2</sub>S and Ag phases. Lou and co-workers<sup>20</sup> have synthesized Ag<sub>2</sub>S–Ag hybrid nanotubes by rapid microwave-assisted

<sup>a</sup>Department of Electrical and Computer Engineering, National University of Singapore, 4 Engineering Drive 3, 117583, Singapore. E-mail: elehgw@nus.edu.sg

<sup>b</sup>Engineering Science Programme, National University of Singapore, 9 Engineering Drive 1, 117575, Singapore

<sup>c</sup>Institute of Materials Research and Engineering, A\*STAR (Agency for Science, Technology and Research), 3 Research Link, 117602, Singapore

<sup>d</sup>Division of Physics and Applied Physics, School of Physical and Mathematical Sciences, Nanyang Technological University, 21 Nanyang Link, 637371, Singapore

† Electronic supplementary information (ESI) available. See DOI: 10.1039/c7ta06473j

sulfidation of  $\text{Ag}_2\text{CO}_3$  nanorods and utilized them for the visible-light photocatalytic degradation of methyl orange and the reduction of aqueous  $\text{Cr}(\text{VI})$ . It should be noted that although the Ag– $\text{Ag}_2\text{S}$  composites have been utilized in various photocatalytic reactions,<sup>19,20,25,31–34</sup> the roles of Ag SPR in the photoactivity enhancement of Ag– $\text{Ag}_2\text{S}$  composites as well as the charge transfer dynamics, to the best of our knowledge, have not been elaborated.

In order to identify the role of Ag SPR in enhancing the photoelectrochemical and photocatalytic performances of Ag– $\text{Ag}_2\text{S}$  composites, herein, we choose one-dimensional (1D) Ag nanowires (NWs) as the interest due to their distinct SPR absorption and the 1D structure-directing advantages.<sup>35</sup> Through an *in situ* controllable and spontaneous sulfidation treatment at room temperature, the Ag NWs can be partially converted to the corresponding  $\text{Ag}_2\text{S}$  semiconductor material, thus leading to the formation of a series of  $\text{Ag}@\text{Ag}_2\text{S}$  composites with intimate interface combined in a uniform coaxial core-shell motif. The coaxial  $\text{Ag}@\text{Ag}_2\text{S}$  composite with an optimized ratio of Ag to  $\text{Ag}_2\text{S}$  exhibits enhanced photoelectrochemical and photocatalytic activities under visible light irradiation. The underlying contribution of Ag SPR to the photoelectrochemical and photocatalytic performance enhancement of the  $\text{Ag}@\text{Ag}_2\text{S}$  hybrids has been elucidated through the controlled wavelength-dependent experiments combined with transient absorption analysis. Importantly, strong correlation between the absorption characteristics and wavelength dependent photochemical properties reveals the predominant SPR contribution of Ag NWs to the enhancement of photoelectrochemical and photocatalytic activities of  $\text{Ag}@\text{Ag}_2\text{S}$  hybrids. In addition, transient absorption spectroscopy provides clear evidence of an ultrafast electron transfer from the Ag core to the  $\text{Ag}_2\text{S}$  shell within  $\sim 350$  fs. Accordingly, a schematic diagram has been presented to illustrate the charge transfer process in the coaxial  $\text{Ag}@\text{Ag}_2\text{S}$  hybrid. This work provides a fundamental understanding and insight into the role of the Ag component in photoelectrochemical and photocatalytic activities enhancement of Ag– $\text{Ag}_2\text{S}$  hybrid nanosystems, which is expected to promote the full utilization of the Ag plasmonic function and thus the design of efficient platforms for solar energy conversion technologies.

## Experimental section

### Materials

Silver nitrate ( $\text{AgNO}_3$ ), poly(vinyl pyrrolidone) (PVP, MW  $\approx 1\,300\,000$ ), iron(III) chloride ( $\text{FeCl}_3$ ), sodium sulfide ( $\text{Na}_2\text{S}$ ), and sulfur powder were all obtained from Sigma-Aldrich and ethylene glycol (EG) was obtained from J. T. Baker. All of the reagents were of analytical grade and used as received without further purification. The deionized water used in all reactions was obtained by filtering through a set of Millipore cartridges (Epure, Dubuque, IA).

### Preparation

**(a) Synthesis of Ag nanowires (NWs).** Ag NWs were synthesized *via* a modified polyol process,<sup>36</sup> which involved the

reduction of silver nitrate ( $\text{AgNO}_3$ ) in the presence of PVP in ethylene glycol (EG). 2 g of  $\text{FeCl}_3$  solution ( $6 \times 10^{-4}$  M in EG), 0.27 g of  $\text{AgNO}_3$ , and 0.1 g of PVP were added to 30 mL of EG. The mixture was stirred for 12 h and then transferred to a Teflon-lined autoclave and heated at 150 °C for 1.5 h. The sample was cooled down to room temperature and then washed with ethanol and acetone to remove excess EG and PVP. After washing, the product was collected by centrifugation at 10 000 rpm for 5 min and then re-dispersed by brief sonication in ethanol (5 mL) and water (25 mL) for the sulfidation reaction with polysulfide ( $\text{Na}_2\text{S}_x$ ).

**(b) Preparation of  $\text{Na}_2\text{S}_x$  aqueous solution.** The  $\text{Na}_2\text{S}_x$  solution was prepared by reacting aqueous  $\text{Na}_2\text{S}$  with sulfur powder.<sup>26</sup> In a typical process, 28 mg of sulfur powder were mixed with 11.7 mL of 50 mM  $\text{Na}_2\text{S}$  aqueous solution in a 20 mL vial. The suspension was agitated by sonication for about 30 min. The vial was then capped and placed in an oven at 80 °C for 12 h. The color of the solution turned bright yellow upon complete dissolution of all the sulfur powder.

**(c) Sulfidation reaction.** In a standard procedure for sulfidation, 0.2 mL of the  $\text{Na}_2\text{S}_x$  solution was added to 30 mL of the suspension of Ag NWs (1.0 mM in terms of elemental silver) at room temperature under magnetic stirring. The reaction was quenched at a specific point in time by centrifuging the solution at 10 000 rpm for 5 min. The product was then washed twice with DI water. The final product was re-dispersed in ethanol for further structural analysis and UV-vis measurements.

### Characterization

Field emission scanning electron microscopy (SEM, JEOL JSM-7001F) was used to determine the morphology of the samples. Transmission electron microscopy (TEM) analysis was performed on a JEOL model JEM 2010 EX instrument at an accelerating voltage of 200 kV. The crystal phase properties of the samples were analyzed with a Bruker D5005 Advance X-ray diffractometer (XRD) using graphite monochromated Cu  $K\alpha$  radiation at  $\lambda = 1.541$  Å. X-ray photoelectron spectroscopy (XPS) measurements were carried out on a Thermo Scientific ESCA Lab250 spectrometer which consists of a monochromatic Al  $K\alpha$  as the X-ray source. All of the binding energies were calibrated by the C 1s peak at 284.6 eV. The optical properties of the samples were analyzed by UV-vis diffuse reflectance spectroscopy (DRS) using a UV-vis spectrophotometer (Shimadzu, UV-3600). The photoelectrochemical analysis was carried out in a conventional three-electrode cell using a Pt plate and an Ag/AgCl electrode as the counter electrode and reference electrode, respectively. The electrolyte was 0.2 M  $\text{Na}_2\text{SO}_4$  aqueous solution without an additive (pH = 6.8). The working electrode was prepared on fluoride tin oxide (FTO) glass. The photocurrent measurements were taken on a CH Instrument workstation. Transient absorption spectroscopy was performed at room temperature using a commercially available Helios™ TA spectrometer (Ultrafast Systems LLC). The laser source was the Coherent Legend regenerative amplifier (150 fs, 1 kHz, 800 nm) seeded by using a Coherent Vitesse oscillator (100 fs, 80 MHz). The 400 nm pump pulses were obtained by frequency doubling

the 800 nm fundamental regenerative amplifier output with a BBO crystal. The white light probe beams were generated by focusing a small portion (around 10  $\mu\text{J}$ ) of the fundamental 800 nm laser pulses into a 2 mm sapphire plate. The probe beam was collected using a dual detector for UV-vis (CMOS sensor).

### Photoactivity testing

10 mg of the sample was dispersed in 20 mL of methyl orange (5 ppm) aqueous solution. The mixture was stirred for 1 h in the dark to blend well and allow the adsorption-desorption equilibrium to be attained before irradiation. A 300 W Xe lamp (Excelitas, PE300BFM) with a light intensity of 100  $\text{mW cm}^{-2}$  equipped with a 400 nm long-pass filter was used as a visible light source. 2 mL of sample solution was drawn from the system at regular time intervals during the experiment and analyzed using a UV-vis spectrophotometer (Shimadzu, UV-3600).

## Results and discussion

The one-dimensional (1D) coaxial  $\text{Ag@Ag}_2\text{S}$  nanowire (NW) hybrids are synthesized by a simple *in situ* sulfidation treatment at room temperature, as illustrated in Fig. 1a. The Ag NWs fabricated by a poly(vinyl pyrrolidone) (PVP)-assisted polyol reduction approach are used as the starting material for the *in situ* formation of the  $\text{Ag}_2\text{S}$  shell. It can be seen from the scanning electron microscopy (SEM) image in Fig. 1b that the polyol-synthesized Ag NWs possess uniform diameters of *ca.* 80 nm and lengths ranging from 5 to 20  $\mu\text{m}$  with a smooth

surface. The Ag NWs fabricated by such a method were reported to possess a pentagonal cross-section with five-fold symmetry.<sup>37</sup> Through controlling the sulfidation reaction time, a series of  $\text{Ag@Ag}_2\text{S}$  NW hybrids with different degrees of sulfidation can be obtained (denoted as  $\text{Ag@Ag}_2\text{S}-x$ ;  $x$  is the sulfidation time). The morphological evolution process of the  $\text{Ag@Ag}_2\text{S}$  NW hybrids has been investigated *via* time-dependent experiments as discussed below.

Fig. S1† and 1c show the SEM images of the 1D  $\text{Ag@Ag}_2\text{S}$  NW hybrids. Taking the sample with a sulfidation reaction time of 40 min as an example (Fig. 1c), it is easy to observe that the 1D morphology of the nanowires is well retained, indicating that the mild sulfidation process has no significant effects on the 1D structure of Ag NWs. As compared with the smooth surface of bare Ag NWs, the surface of  $\text{Ag@Ag}_2\text{S}$  NW hybrids becomes rough, especially for the samples with sulfidation reaction times of 40 min and 60 min, as revealed in Fig. 1c and S1d,† respectively. This should be ascribed to the formation of the  $\text{Ag}_2\text{S}$  component on the surface of Ag NWs. The energy-dispersive X-ray (EDX) analysis has been carried out for Ag NWs and the  $\text{Ag@Ag}_2\text{S}$  NW hybrids. As shown in Fig. 1d, with increasing the sulfidation time, the atomic percentage of Ag gradually decreases and simultaneously the content of S increases correspondingly. Notably, there is no significant difference in the diameters of Ag NWs and  $\text{Ag@Ag}_2\text{S}-40$  (as an example), as reflected by the histograms in Fig. 1e. These results further confirm that the Ag NWs are partially converted to  $\text{Ag}_2\text{S}$  *via* an *in situ* process. Fig. 1f displays the X-ray diffraction (XRD) patterns of the  $\text{Ag@Ag}_2\text{S}$  NW hybrids. Only the diffraction peaks of face-centered cubic Ag (JCPDS card no. 87-0720; space group:

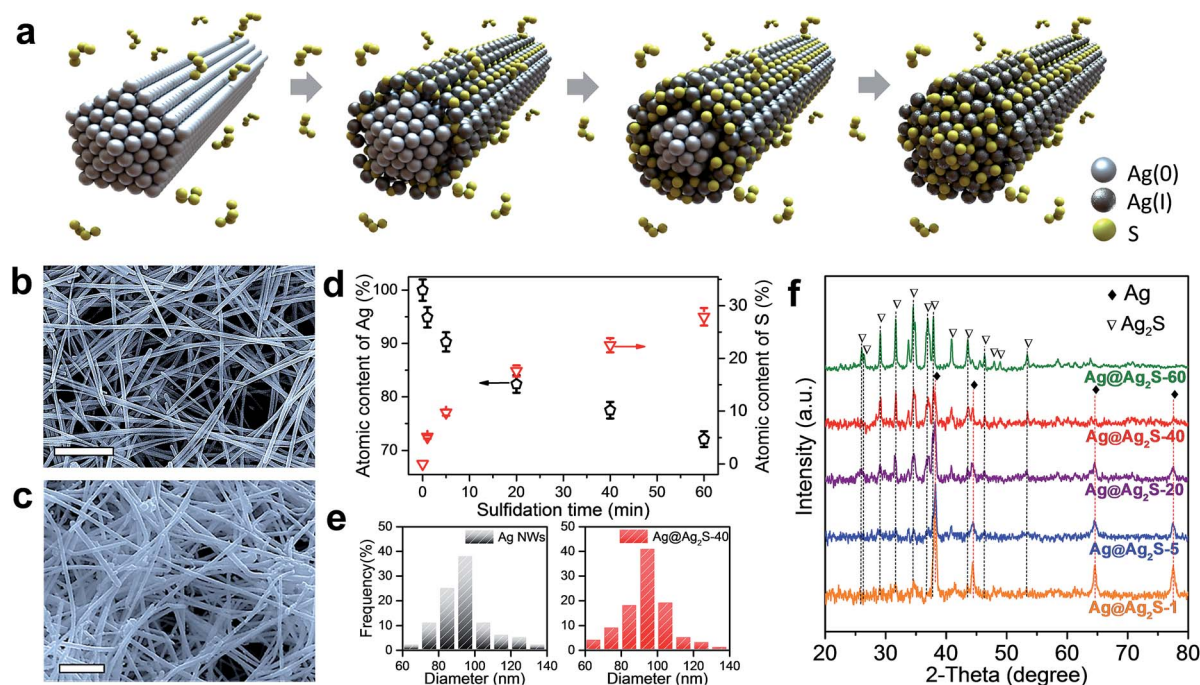


Fig. 1 (a) Schematic illustration for the preparation of  $\text{Ag@Ag}_2\text{S}$  composites using Ag nanowires (NWs) as the starting material; SEM images of (b) Ag NWs, and (c)  $\text{Ag@Ag}_2\text{S}-40$  composite (the scale bar is 1  $\mu\text{m}$ ); (d) atomic content evolution of Ag and S along with the sulfidation time; (e) the diameter distribution histograms of Ag and  $\text{Ag@Ag}_2\text{S}-40$  NWs; (f) XRD patterns of Ag NWs and  $\text{Ag@Ag}_2\text{S}$  composites.



$Fm\bar{3}m$ ,  $a = b = c = 4.077$ ) are observed for the samples with short sulfidation time, *i.e.*, Ag@Ag<sub>2</sub>S-1 and Ag@Ag<sub>2</sub>S-5, as marked by rhombuses. As the reaction time increases, the diffraction peaks of monoclinic Ag<sub>2</sub>S (JCPDS card no. 14-0072; space group:  $P2_1/n$ ,  $a = 4.229$  Å,  $b = 6.931$  Å, and  $c = 9.091$  Å) appear as marked by inverted triangles and the intensity becomes stronger, while the diffraction peaks of Ag become weaker at the same time and eventually disappear when the sulfidation time reaches 60 min due to the low content of Ag NWs in the Ag@Ag<sub>2</sub>S hybrids. The average crystallite size of Ag<sub>2</sub>S has been calculated according to the Scherrer formula based on the XRD pattern. Taking Ag@Ag<sub>2</sub>S-60 as an example due to its most distinct diffraction peaks of monoclinic Ag<sub>2</sub>S, the peak width of half-height (FWHM) of the Ag<sub>2</sub>S (−112) peak can be obtained by fitting to a Lorentzian function (Fig. S2†). Accordingly, the estimated average crystallite size of Ag<sub>2</sub>S is about 21.5 nm, which is beyond the quantum-confinement regime.<sup>38–40</sup> Besides, no additional peaks of other crystalline phases were detected, indicating the high purity of the samples. Obviously, these results demonstrate that the gradual conversion of Ag NWs to Ag@Ag<sub>2</sub>S hybrids can be achieved by this controllable sulfidation method at room temperature.

To further elucidate the microscopic morphology evolution during the sulfidation process, transmission electron microscopy (TEM) analysis has been performed. The TEM image of bare Ag NWs (Fig. 2a) shows the 1D morphology with a smooth surface. The identified lattice spacing of 0.204 nm in the high-resolution TEM (HRTEM) image (Fig. 2e) corresponds to the (200) facet of Ag. The selected-area electron diffraction (SAED) pattern in the inset of Fig. 2a displays relatively weak diffraction

spots along one direction (as indicated by the red lines), which is consistent with previous reports of pentagonally twinned silver NWs.<sup>41</sup> For the sample obtained with sulfidation for 5 min, a thin layer of Ag<sub>2</sub>S is formed on the surface of the Ag NWs (Fig. 2b). The diffraction spots of Ag NWs and weak diffraction rings of Ag<sub>2</sub>S can both be observed in the SAED pattern. As the sulfidation time increases, the Ag<sub>2</sub>S layer becomes thicker. For example, as for the sample of Ag@Ag<sub>2</sub>S-40, a well-defined core-shell structure is formed (Fig. 2c) and the lattice spacing of 0.261 nm in the shell region (Fig. 2f) is ascribed to the (121) facet of monoclinic Ag<sub>2</sub>S. Besides, clear diffraction rings are identified and indexed to the monoclinic Ag<sub>2</sub>S. After sulfidation for 60 min, a thicker Ag<sub>2</sub>S shell is formed, as reflected by the TEM and SAED images (Fig. 2d). The SAED results of these samples with different sulfidation reaction time periods are in good agreement with the XRD spectra (Fig. 1e). To further corroborate the elemental distribution of the 1D Ag@Ag<sub>2</sub>S core-shell structure, elemental mapping has been performed on Ag@Ag<sub>2</sub>S-40 as a typical example. The results are shown in Fig. 2g. We can see that the Ag NWs are located in the core area, while the Ag<sub>2</sub>S layer forms the shell, confirming the formation of the Ag@Ag<sub>2</sub>S core-shell structure, which is also evidenced by the line-scan profile. The above results clearly demonstrate the morphology evolution from Ag NWs to the coaxial Ag@Ag<sub>2</sub>S core-shell structure during the mild sulfidation process.

Fig. S3a† shows the Ag 3d X-ray photoelectron spectroscopy (XPS) spectra of Ag NWs. The two typical peaks located at about 368.2 eV and 374.2 eV can be attributed to the metallic Ag 3d<sub>5/2</sub> and 3d<sub>3/2</sub> binding energies, respectively.<sup>19,20</sup> As for the Ag@Ag<sub>2</sub>S-

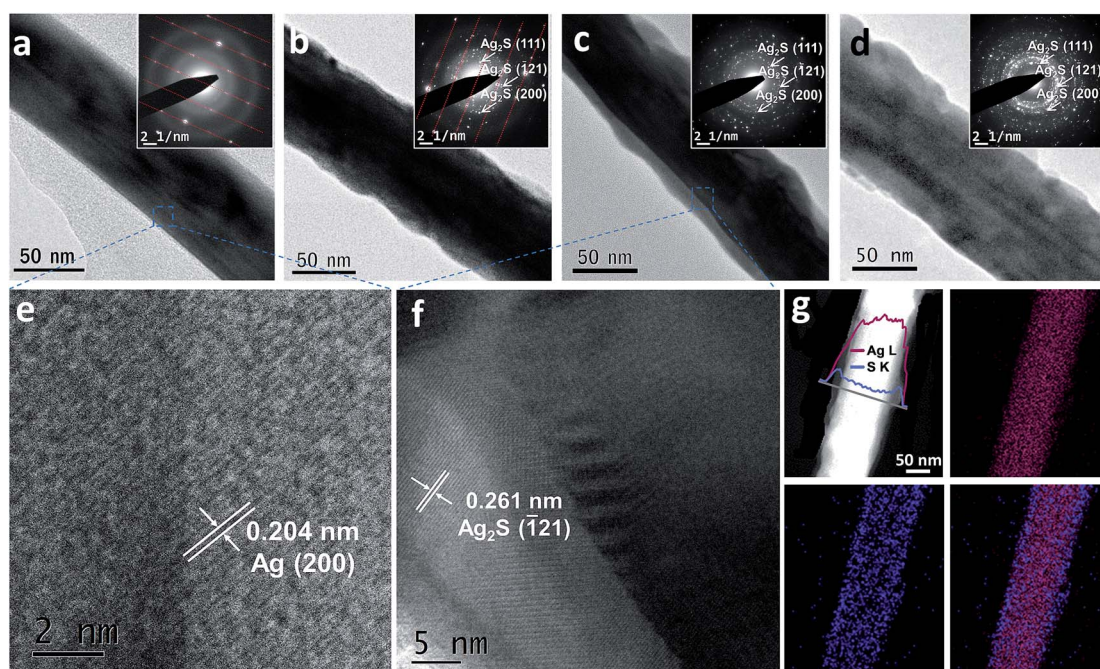


Fig. 2 TEM images of (a) Ag NWs, (b) Ag@Ag<sub>2</sub>S-5, (c) Ag@Ag<sub>2</sub>S-40 and (d) Ag@Ag<sub>2</sub>S-60 (the insets are the corresponding SAED patterns); HRTEM images of (e) Ag NWs, and (f) Ag@Ag<sub>2</sub>S-40; (g) high-angle annular dark-field scanning transmission electron microscopy (HAADF-STEM) image (the inset is the line-scan profile) and the corresponding elemental mapping results of the Ag@Ag<sub>2</sub>S-40 composite.

40 composite, the Ag  $3d_{5/2}$  and  $3d_{3/2}$  peaks are shifted to 367.8 eV and 373.8 eV, respectively, which are indexed to Ag(I) of  $Ag_2S$  (Fig. S3b†).<sup>20</sup> In the S 2p XPS spectrum shown in Fig. S3c,† the peaks at 161.2 eV and 162.4 eV correspond to the binding energies of S  $2p_{3/2}$  and  $2p_{1/2}$ , respectively, indicating that the valance state of element S is  $-2$ .<sup>19</sup> It is well known that XPS is a useful technique to analyze the surface composition of samples and its detectable depth is no more than 10 nm.<sup>42</sup> We can see from the TEM images that the  $Ag_2S$  outer shell is thicker than 10 nm and the Ag NWs are encapsulated by the  $Ag_2S$  shell. Therefore, it is reasonable that no characteristic peaks of metallic Ag in the core are detected in the XPS spectra of the  $Ag@Ag_2S$ -40 composite. The combined analysis of SEM, TEM, elemental mapping and XPS results confirms the formation of the coaxial  $Ag@Ag_2S$  core-shell structure *via* such a facile route at room temperature.

The optical properties of the samples are displayed in Fig. 3a. The bare Ag NWs exhibit two absorbance peaks at 350 and 385 nm, which are attributed to the out-of-plane quadrupole resonance and the transverse SPR of Ag NWs, respectively.<sup>43</sup> It is well known that the SPR absorption peak is highly sensitive to the optical and electronic properties of the surrounding medium.<sup>44,45</sup> The optical response of the Ag NWs is observed to be markedly affected by the formation of the  $Ag_2S$  shell. Upon the formation of the  $Ag_2S$  shell, the quadrupole resonance of Ag NWs gradually decreases, and there is a broad peak ranging from 400 to 800 nm for the  $Ag@Ag_2S$  sample, which undergoes a red-shift with the increase of sulfidation time. Notably, in the present work, pure  $Ag_2S$  NWs cannot be obtained using the *in situ* sulfidation treatment even prolonging the reaction time to 24 h with an excessive sulfur source. This is because when the relatively thick  $Ag_2S$  shell forms, it will prevent further sulfidation reaction with the Ag NW core, thus leading to the inaccessibility of the pure  $Ag_2S$  NW counterpart for investigating its optical properties for comparison. It can be learnt from the

literature that 1D  $Ag_2S$  NWs with the average diameter of *ca.* 80–100 nm exhibit no obvious absorption peaks in the range of 400–800 nm.<sup>46,47</sup> Besides, there is no strong quantum-confinement effect for the  $Ag_2S$  due to its relatively large crystallite size,<sup>38–40</sup> as demonstrated by the analysis of the XRD results. Therefore, the broad peaks observed for  $Ag@Ag_2S$  NWs should be ascribed to the SPR absorption of Ag. This result can be further verified by the simulated extinction spectra. As shown in Fig. S4,† the coating of the  $Ag_2S$  shell leads to a significant red-shift of the transverse SPR band of Ag NWs due to the relatively high dielectric constant of  $Ag_2S$ .<sup>26</sup> The variety of diameter, length and the  $Ag_2S$  shell thickness for  $Ag@Ag_2S$  hybrids should be responsible for the broad peaks of Ag SPR. The broad absorbance from the UV to the near-infrared window is crucial for the full use of sunlight.

Then we investigated the photoelectrochemical performance of  $Ag@Ag_2S$  hybrids as well as Ag NWs under visible light irradiation ( $\lambda > 400$  nm). Fig. 3b shows the transient photocurrent responses of the samples with the illumination of visible light under zero bias condition. The photocurrent response from the bare Ag NWs electrode under visible light irradiation is very weak, indicating that there is no efficient electron extraction under the present conditions.<sup>48,49</sup> Notably, the formation of the  $Ag_2S$  shell is able to promote the photocurrent response. As the content of  $Ag_2S$  increases by prolonging the sulfidation time, the photocurrent density is gradually enhanced. When the sulfidation time is 40 min, the optimal photocurrent performance can be obtained. With prolonging the sulfidation time to 60 min, the photocurrent density decreases. The photocurrent as a function of applied voltage of these samples has also been evaluated. As displayed in Fig. 3c,  $Ag@Ag_2S$  hybrids with different ratios of Ag to  $Ag_2S$  exhibit tunable photocurrent response. The enhanced photoelectrochemical performances of  $Ag@Ag_2S$  composites indicate a more efficient separation and transfer of photogenerated charge carriers achieved in the  $Ag@Ag_2S$  samples. These results manifest that there should be a synergistic effect between Ag and  $Ag_2S$  with intimate interfacial contact.

In addition, the visible-light ( $\lambda > 400$  nm) photocatalytic activities of the samples have been evaluated by the degradation of organic dye, methyl orange (MO), one of the most commonly used probe reactions in the heterogeneous photocatalysis.<sup>20,50,51</sup> It is seen from Fig. 3d that the bare Ag NWs exhibit no photoactivity under the present conditions, which is due to the fact that for the bare Ag NWs, the hot electrons are unable to be effectively generated and extracted for participating in the surface reaction.<sup>48,49,52,53</sup> This is consistent with its photoelectrochemical performance. In addition, the lack of photoactivity can also exclude the possibility of thermochemical degradation of the organic compounds induced by the localized heating effect resulting from the SPR of Ag NWs.<sup>54</sup> The partial conversion of Ag to  $Ag_2S$  can impart the composite with visible-light photoactivity. In particular, the  $Ag@Ag_2S$ -40 composite exhibits the optimum photocatalytic activities. After the reaction for 180 min under visible light irradiation, almost 95% of MO is removed over  $Ag@Ag_2S$ -40 (Fig. S5†). Further increasing the sulfidation reaction time leads to the deterioration of

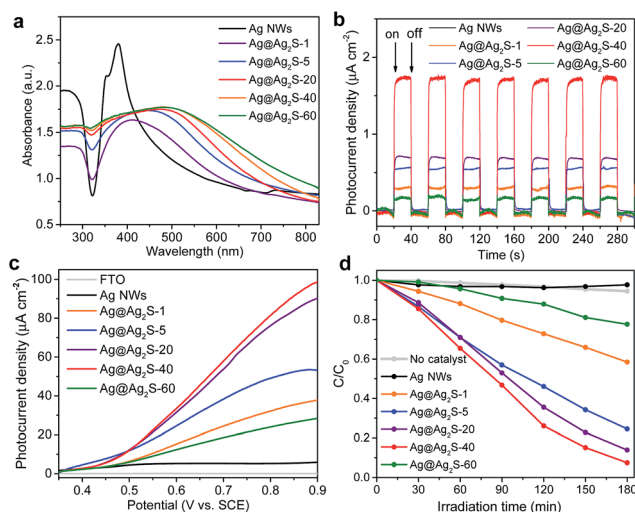


Fig. 3 (a) UV-vis absorption spectra of Ag NWs and  $Ag@Ag_2S$  composites; (b) transient photocurrent responses, (c) photocurrent–voltage curves, and (d) photoactivity towards the degradation of MO of the samples under visible light irradiation ( $\lambda > 400$  nm).

photoactivity, as observed in the Ag@Ag<sub>2</sub>S-60 sample. These results along with the photoelectrochemical performance demonstrate that the synergistic effect between Ag and Ag<sub>2</sub>S reaches the optimum when the sulfidation reaction time is 40 min. The pseudo-first order fitting results (Fig. S6†) reveal that the pseudo-first order constant  $k$  of Ag@Ag<sub>2</sub>S-40 is the highest at 0.01233 min<sup>-1</sup>. A blank experiment in the absence of photocatalyst exhibits no photodegradation activity, indicating that the reaction over Ag@Ag<sub>2</sub>S hybrids is driven by photocatalytic redox processes.

In an effort to better understand the role of Ag SPR in enhancing the photoelectrochemical and photocatalytic activities, the performances of the optimal sample Ag@Ag<sub>2</sub>S-40 have been analyzed under the irradiation of different monochromatic lights in the wavelength range of 400–700 nm. The intensity of different monochromatic lights has been normalized. Fig. 4a exhibits the transient photocurrent responses of Ag@Ag<sub>2</sub>S-40 under different monochromatic irradiation conditions. It is observed that the Ag@Ag<sub>2</sub>S-40 exhibits photocurrent under the visible light irradiation ranging from 400 to 700 nm. Among the different incident wavelengths, the photocurrent density is the highest when the monochromatic irradiation is centered at 475 nm. The average photocurrent density under different LED irradiation conditions resembles the light absorption spectrum of Ag@Ag<sub>2</sub>S-40, as shown in Fig. 4b. It is known that the photocurrent is formed mainly by the diffusion of the photogenerated electrons to the back contact.<sup>55,56</sup> Therefore, the conformity of the photocurrent and the SPR absorption of Ag indicates that the electrons photogenerated from Ag should be responsible for the enhanced photoelectrochemical performance of Ag@Ag<sub>2</sub>S composites.

The photocatalysis action spectra of Ag@Ag<sub>2</sub>S-40 have also been obtained by plotting the apparent kinetics as a function of the wavelength of incident monochromatic light in the wavelength range of 400–700 nm. We can see from Fig. 4c and d that

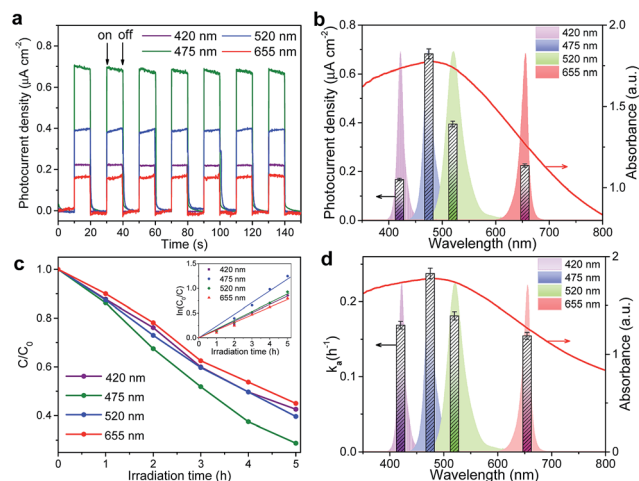


Fig. 4 (a) Photoelectrochemical performance and (c) photocatalytic activity of the Ag@Ag<sub>2</sub>S-40 composite towards the degradation of MO under different monochromatic light irradiation conditions, and (b, d) the corresponding action spectra.

the photoactivity of Ag@Ag<sub>2</sub>S-40 depends strongly on the irradiation wavelength and qualitatively tracks the absorption spectrum. The action and absorption spectra coincide in their peak positions, *ca.* 475 nm. The highest rate enhancement observed at 475 nm corresponds to the SPR peak of metallic Ag, which clearly suggests that the excitation of SPR of the Ag component contributes to the observed photoactivity enhancement of Ag@Ag<sub>2</sub>S-40 under visible light irradiation. These qualitative mapping results between the photoelectrochemical/photocatalytic activity and the absorption spectrum of Ag@Ag<sub>2</sub>S-40 clearly demonstrate that the enhancement of photoelectrochemical and photocatalytic performances of Ag@Ag<sub>2</sub>S-40 is closely related to the SPR absorption of the Ag component.

We employed transient absorption (TA) spectroscopy to analyze the electron transfer kinetics in the samples. Fig. 5a and b show the TA spectra of Ag NWs and Ag@Ag<sub>2</sub>S-40 NWs recorded within 1 ps following 400 nm excitation. A photoinduced absorption (PIA, *i.e.*, positive  $\Delta A$ ) band is observed in the range from  $\sim 415$  nm to 500 nm for Ag NWs in ethanol solvent, which demonstrates a similar behavior with the previously reported TA spectra of Ag nanoparticles.<sup>57,58</sup> It can be seen from Fig. 5c that the transient kinetics of Ag NWs probed at 420 nm have an instantaneous buildup with the rise time of  $\sim 150$  fs (comparable to the pump pulse duration), which implies an instantaneous excitation of valence electrons *via* plasmon resonance. The TA signal relaxation is dominated by a fast decay (with a lifetime of  $\sim 900$  fs) due to the hot-electron relaxations *via* electron–electron and electron–phonon scatterings, then followed by a slower decay ( $\sim 100$  ps, as shown in Fig. 5d) arising from the phonon–phonon and phonon–solvent interactions.<sup>57,58</sup>

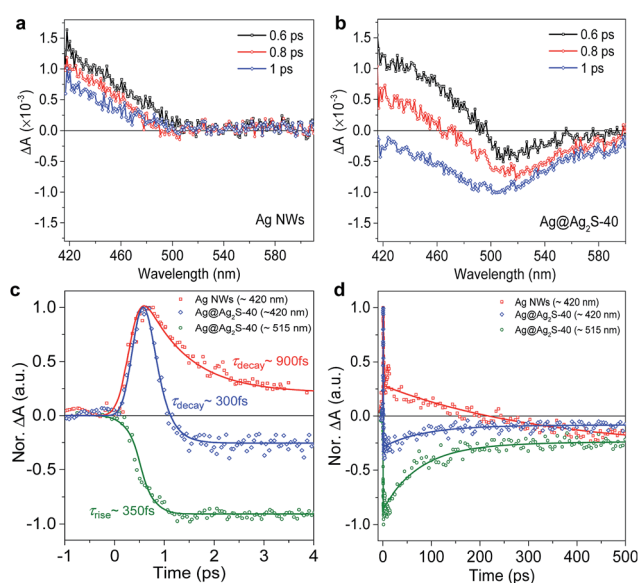


Fig. 5 Transient absorption (TA) spectra of (a) Ag NWs and (b) Ag@Ag<sub>2</sub>S-40 NWs dispersed in ethanol solvent at different delay times after 400 nm photoexcitation with a pump fluence of 15  $\mu\text{J cm}^{-2}$ ; normalized TA kinetics probed at different wavelengths for Ag NWs and Ag@Ag<sub>2</sub>S-40 NWs plotted over the (c) short and (d) long time windows, respectively; solid lines are exponential fits.



In contrast, after Ag NWs are covered with the Ag<sub>2</sub>S shell, the TA spectra show a faster reduction of the PIA signal (from Ag) superimposed with an increase in broad photobleaching (PB, *i.e.*, negative  $\Delta A$ ) band that peaked around  $\sim 515$  nm (Fig. 5b). The PB peak position is consistent with the absorption peak in the linear absorption spectrum and can be attributed to the state-filling induced by the injected electrons of Ag<sub>2</sub>S shells. The fitted buildup time of the PB peak is  $\sim 350$  fs (Fig. 5c), which is close to the fast decay time of the PIA signal probed at  $\sim 420$  nm, and can therefore be attributed to the electron transfer time from the Ag core to the Ag<sub>2</sub>S shell. The subsequent slower decay with  $\sim 200$  ps lifetime (Fig. 5d) can be attributed to the relaxation of electrons from the conduction band of Ag<sub>2</sub>S. Accordingly, the TA spectra provide clear evidence of the ultrafast electron transfer from the Ag NW core to the Ag<sub>2</sub>S shell, which facilitates the efficient charge collection and separation in this hybrid system. These results together with the photoelectrochemical/photocatalytic activity action spectra highlight the essential role of Ag SPR in enhancing the performance of Ag@Ag<sub>2</sub>S NW hybrids.

Accordingly, the charge transfer process of Ag@Ag<sub>2</sub>S composites has been schematically proposed. As illustrated in Fig. 6, Ag NWs and Ag<sub>2</sub>S can be both excited under visible light irradiation. The work function of Ag and the bottom of the conduction band of Ag<sub>2</sub>S are located at  $-4.26$  eV and  $-4.42$  eV from the vacuum energy level, respectively.<sup>19,20</sup> Therefore, due to the SPR effect of Ag NWs and the matched band structure of the two components, with the illumination of visible light, the hot electrons will inject into the Ag<sub>2</sub>S shell from Ag NWs, which has been confirmed by the transient absorption analysis.

Besides, the photostability of Ag@Ag<sub>2</sub>S-40 has been investigated *via* recycling photoactivity experiments. The results (Fig. S7†) show that throughout the five-time recycle test for the degradation of MO under visible-light irradiation, there is no significant loss in the photoactivity of Ag@Ag<sub>2</sub>S-40, indicating its good photostability.

As discussed above, the pure Ag<sub>2</sub>S NWs cannot be achieved through the present *in situ* sulfidation method probably due to the fact that further sulfidation reaction is prevented by the as-

formed Ag<sub>2</sub>S shell. This results in the inaccessibility of the pure Ag<sub>2</sub>S NW counterpart as well as the performance comparison of Ag<sub>2</sub>S NWs with the Ag@Ag<sub>2</sub>S composites. In spite of such a situation, the photoelectrochemical/photocatalytic activity action spectra and transient absorption results definitely reveal that the SPR phenomenon of Ag NWs plays an essential role in enhancing the performance of Ag@Ag<sub>2</sub>S hybrids, which is often overlooked in previous reports related to the Ag–Ag<sub>2</sub>S photo-catalytic systems.<sup>19,20,25,31–34</sup> The identification of the contribution from Ag SPR towards enhancing the photoelectrochemical and photocatalytic performances of Ag-based composites enables us to fully understand the role of Ag in the hybrid systems and thus to take better advantage of the metal components for target applications.

## Conclusions

In summary, a series of 1D Ag@Ag<sub>2</sub>S core-shell hybrids have been prepared through an *in situ* controllable and spontaneous sulfidation treatment at room temperature. The coaxial Ag@Ag<sub>2</sub>S composites with an optimized ratio of Ag to Ag<sub>2</sub>S exhibit enhanced photoelectrochemical and photocatalytic performances under visible light irradiation. The action spectral analysis using different monochromatic lights has been performed to identify the role of Ag SPR in the performance enhancement of Ag@Ag<sub>2</sub>S composites. The results reveal that the photoelectrochemical and photocatalytic activities of the optimum Ag@Ag<sub>2</sub>S-40 depend strongly on the wavelength and qualitatively track its absorption spectrum. Such observation clearly suggests that the excitation of SPR of the Ag component contributes to the visible-light activities enhancement of Ag@Ag<sub>2</sub>S-40. In addition, transient absorption spectroscopy provides direct evidence of the ultrafast electron transfer from the Ag NW core to the Ag<sub>2</sub>S shell. Accordingly, the charge transfer process of Ag@Ag<sub>2</sub>S composites has been schematically proposed. This work is expected to provide a fundamental understanding and insight into the role of the Ag component in photoelectrochemical and photocatalytic activity enhancement of Ag–Ag<sub>2</sub>S hybrid nanosystems, based on which the plasmonic function of Ag will be exploited better to design more efficient solar-energy-conversion systems.

## Conflicts of interest

There are no conflicts of interest to declare.

## Acknowledgements

This research is supported by the Singapore National Research Foundation (NRF), under the Energy Innovation Research Programme (EIRP) R-263-000-B82-279, managed on behalf of the Building and Construction Authority (BCA). T. C. S. acknowledges the financial support from the Ministry of Education Academic Research Fund Tier 1 grant M4011769 and Tier 2 grant MOE2016-T2-1-034 and from NRF through the Competitive Research Program NRF-CRP14-2014-03.

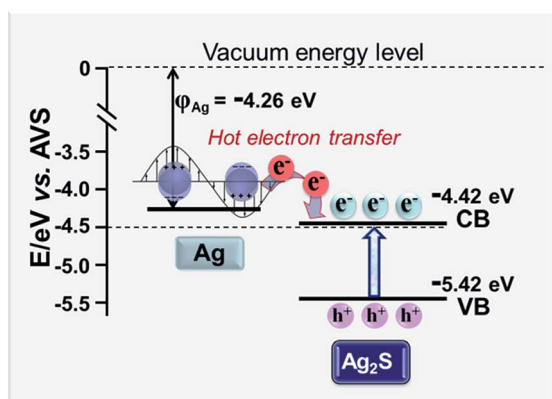


Fig. 6 The schematic illustration of the charge transfer process in Ag@Ag<sub>2</sub>S hybrids; AVS is short for the absolute vacuum scale.

## References

- 1 L. Zhang, D. A. Blom and H. Wang, *Chem. Mater.*, 2011, **23**, 4587–4598.
- 2 R. Costi, A. E. Saunders and U. Banin, *Angew. Chem., Int. Ed.*, 2010, **49**, 4878–4897.
- 3 T. Mokari, C. G. Sztrum, A. Salant, E. Rabani and U. Banin, *Nat. Mater.*, 2005, **4**, 855–863.
- 4 R. Jiang, B. Li, C. Fang and J. Wang, *Adv. Mater.*, 2014, **26**, 5274–5309.
- 5 U. Banin, Y. Ben-Shahar and K. Vinokurov, *Chem. Mater.*, 2014, **26**, 97–110.
- 6 Y. K. Lee, C. H. Jung, J. Park, H. Seo, G. A. Somorjai and J. Y. Park, *Nano Lett.*, 2011, **11**, 4251–4255.
- 7 M. W. Knight, H. Sobhani, P. Nordlander and N. J. Halas, *Science*, 2011, **332**, 702–704.
- 8 W. Dong, Y. Li, D. Niu, Z. Ma, J. Gu, Y. Chen, W. Zhao, X. Liu, C. Liu and J. Shi, *Adv. Mater.*, 2011, **23**, 5392–5397.
- 9 J. Qi, X. Dang, P. T. Hammond and A. M. Belcher, *ACS Nano*, 2011, **5**, 7108–7116.
- 10 S. Linic, P. Christopher and D. B. Ingram, *Nat. Mater.*, 2011, **10**, 911–921.
- 11 Y. Sun, *Nanoscale*, 2010, **2**, 1626–1642.
- 12 K. E. Korte, S. E. Skrabalak and Y. Xia, *J. Mater. Chem.*, 2008, **18**, 437–441.
- 13 D. B. Ingram and S. Linic, *J. Am. Chem. Soc.*, 2011, **133**, 5202–5205.
- 14 D. Lin, H. Wu, R. Zhang and W. Pan, *Chem. Mater.*, 2009, **21**, 3479–3484.
- 15 Y. Bi, H. Hu, S. Ouyang, Z. Jiao, G. Lu and J. Ye, *J. Mater. Chem.*, 2012, **22**, 14847–14850.
- 16 J. T. Li, S. K. Cushing, J. Bright, F. K. Meng, T. R. Senty, P. Zheng, A. D. Bristow and N. Q. Wu, *ACS Catal.*, 2013, **3**, 47–51.
- 17 Y. Tang, Z. Jiang, G. Xing, A. Li, P. D. Kanhere, Y. Zhang, T. C. Sum, S. Li, X. Chen, Z. Dong and Z. Chen, *Adv. Funct. Mater.*, 2013, **23**, 2932–2940.
- 18 X. Cao, L. Gu, L. Zhuge, W. Gao, W. Wang and S. Wu, *Adv. Funct. Mater.*, 2006, **16**, 896–902.
- 19 M. Pang, J. Hu and H. C. Zeng, *J. Am. Chem. Soc.*, 2010, **132**, 10771–10785.
- 20 W. Yang, L. Zhang, Y. Hu, Y. Zhong, H. B. Wu and X. W. Lou, *Angew. Chem., Int. Ed.*, 2012, **51**, 11501–11504.
- 21 C. Fang, Y. H. Lee, L. Shao, R. Jiang, J. Wang and Q.-H. Xu, *ACS Nano*, 2013, **7**, 9354–9365.
- 22 C. An, S. Peng and Y. Sun, *Adv. Mater.*, 2010, **22**, 2570–2574.
- 23 P. Wang, B. Huang, Y. Dai and M.-H. Whangbo, *Phys. Chem. Chem. Phys.*, 2012, **14**, 9813–9825.
- 24 P. Wang, B. Huang, X. Qin, X. Zhang, Y. Dai, J. Wei and M.-H. Whangbo, *Angew. Chem., Int. Ed.*, 2008, **47**, 7931–7933.
- 25 J. Xiong, C. Han, W. Li, Q. Sun, J. Chen, S. Chou, Z. Li and S. Dou, *CrystEngComm*, 2016, **18**, 930–937.
- 26 J. Zeng, J. Tao, D. Su, Y. Zhu, D. Qin and Y. Xia, *Nano Lett.*, 2011, **11**, 3010–3015.
- 27 M. M. Shahjamali, Y. Zhou, N. Zaree, C. Xue, J. Wu, N. Large, C. M. McGuirk, F. Boey, V. Dravid, Z. Cui, G. C. Schatz and C. A. Mirkin, *ACS Nano*, 2016, **10**, 5362–5373.
- 28 W. P. Lim, Z. Zhang, H. Y. Low and W. S. Chin, *Angew. Chem., Int. Ed.*, 2004, **43**, 5685–5689.
- 29 D. Ayodhya and G. Veerabhadram, *J. Photochem. Photobiol., B*, 2016, **157**, 57–69.
- 30 W. J. Mir, A. Swarnkar, R. Sharma, A. Katti, K. V. Adarsh and A. Nag, *J. Phys. Chem. Lett.*, 2015, **6**, 3915–3922.
- 31 Y. Li, X. Ye, Y. Ma and L. Qi, *Small*, 2015, **11**, 1183–1188.
- 32 S. Xiong, B. Xi, K. Zhang, Y. Chen, J. Jiang, J. Hu and H. C. Zeng, *Sci. Rep.*, 2013, **3**, 2177.
- 33 X. Ma, Y. Zhao, X. Jiang, W. Liu, S. Liu and Z. Tang, *ChemPhysChem*, 2012, **13**, 2531–2535.
- 34 F. Jiang, Q. Tian, M. Tang, Z. Chen, J. Yang and J. Hu, *CrystEngComm*, 2011, **13**, 7189–7193.
- 35 S. Liu, Z.-R. Tang, Y. Sun, J. C. Colmenares and Y.-J. Xu, *Chem. Soc. Rev.*, 2015, **44**, 5053–5075.
- 36 C. F. Tan, W. L. Ong and G. W. Ho, *ACS Nano*, 2015, **9**, 7661–7670.
- 37 Y. Sun, B. Mayers, T. Herricks and Y. Xia, *Nano Lett.*, 2003, **3**, 955–960.
- 38 Y. Du, B. Xu, T. Fu, M. Cai, F. Li, Y. Zhang and Q. Wang, *J. Am. Chem. Soc.*, 2010, **132**, 1470–1471.
- 39 Q. Wang and D.-K. Seo, *Chem. Mater.*, 2006, **18**, 5764–5767.
- 40 Y. Zhang, Y. Liu, C. Li, X. Chen and Q. Wang, *J. Phys. Chem. C*, 2014, **118**, 4918–4923.
- 41 E. C. Garnett, W. Cai, J. J. Cha, F. Mahmood, S. T. Connor, M. Greyson Christoforo, Y. Cui, M. D. McGehee and M. L. Brongersma, *Nat. Mater.*, 2012, **11**, 241–249.
- 42 N. Zhang, S. Liu, X. Fu and Y.-J. Xu, *J. Mater. Chem.*, 2012, **22**, 5042–5052.
- 43 V. Brozek, V. Sember, M. Hrabovsky, J. Janca and J. Domlatil, *Acta Tech. CSAV*, 2007, **52**, 357–364.
- 44 S. Peng, J. M. McMahon, G. C. Schatz, S. K. Gray and Y. Sun, *Proc. Natl. Acad. Sci. U. S. A.*, 2010, **107**, 14530–14534.
- 45 K. L. Kelly, E. Coronado, L. L. Zhao and G. C. Schatz, *J. Phys. Chem. B*, 2003, **107**, 668–677.
- 46 S. Yan, H. Wang, Y. Zhang, S. Li and Z. Xiao, *J. Non-Cryst. Solids*, 2008, **354**, 5559–5562.
- 47 N. Du, H. Zhang, H. Sun and D. Yang, *Mater. Lett.*, 2007, **61**, 235–238.
- 48 C. Clavero, *Nat. Photonics*, 2014, **8**, 95–103.
- 49 C. Han, Q. Quan, H. M. Chen, Y. Sun and Y.-J. Xu, *Small*, 2017, **13**, 1602947.
- 50 A. B. Djurisic, Y. H. Leung and A. M. Ching Ng, *Mater. Horiz.*, 2014, **1**, 400–410.
- 51 Z. Tian, C. Liang, J. Liu, H. Zhang and L. Zhang, *J. Mater. Chem.*, 2012, **22**, 17210–17214.
- 52 M. L. Brongersma, N. J. Halas and P. Nordlander, *Nat. Nanotechnol.*, 2015, **10**, 25–34.
- 53 R. Long, Y. Li, L. Song and Y. Xiong, *Small*, 2015, **11**, 3873–3889.
- 54 M. Rycenga, C. M. Cobley, J. Zeng, W. Li, C. H. Moran, Q. Zhang, D. Qin and Y. Xia, *Chem. Rev.*, 2011, **111**, 3669–3712.



- 55 S. Soedergren, A. Hagfeldt, J. Olsson and S.-E. Lindquist, *J. Phys. Chem.*, 1994, **98**, 5552–5556.
- 56 N. Zhang, Y. Zhang, X. Pan, X. Fu, S. Liu and Y.-J. Xu, *J. Phys. Chem. C*, 2011, **115**, 23501–23511.
- 57 J. H. Hodak, I. Martini and G. V. Hartland, *J. Phys. Chem. B*, 1998, **102**, 6958–6967.
- 58 T. W. Roberti, B. A. Smith and J. Z. Zhang, *J. Chem. Phys.*, 1995, **102**, 3860–3866.